



Research article

The analysis of shrink-fit connection – the methods of heating and the factors influencing the distribution of residual stresses



Roman Król^{a,*}, Zbigniew Siemiątkowski^b

^a Department of Mechanics, Institute of Applied Mechanics and Energetics, Kazimierz Pulaski University of Technology and Humanities in Radom, ul. Stasięckiego 54, Radom, 26-600, Poland

^b Department of Mechanical Technologies, Institute of Machine Design, Kazimierz Pulaski University of Technology and Humanities in Radom, ul. Stasięckiego 54, Radom, 26-600, Poland

ARTICLE INFO

Keywords:

Civil engineering
 Mechanical engineering
 Construction engineering
 Heat exchanger
 Heat transfer
 Automotive engineering
 Machine design
 Tribology
 Strain
 Materials safety
 Crankshaft
 Finite element method
 Shrink-fit connection
 Simulation
 Computational mechanics
 Computer aided design
 Steel construction
 Ship engines

ABSTRACT

The main aim of this article is to compare various heating methods of the shrink-fit connection and to analyse its shrinkage mechanism. The shrink fit connection consists of the crank and the pin or the ring and the pin, which have negative value of the geometrical clearance. The experimental part of research included the measurement of the temperature at the various points in the surface of the crank, the measurement of the residual stress 5 mm from the crank hole and the measurement of the maximum torsional moment, at which sliding of the shrink-fit connection occurs. Conformity between data from the Finite Element Analysis and the experimental data was obtained in relation to the von Mises stress. The analysis results show that Lamé equations can be successfully used for calculation of the load capacity even for parts with the irregular shape.

1. Introduction

Shrink-fit connections are widely used in machine design. It is the very old method of connecting an assembly parts [1]. Current research consider using shrink-fit connections in the reactor vessels of the nuclear power plants [2], in gear mechanism's parts [3, 4] and in crank shafts of ships [5, 6, 7]. In the papers [3, 8, 9], the Finite Element Method (FEM) is used for the analysis of the shrink-fit connections. Numerical methods are often being verified using the theoretical methods based on the axisymmetric Lamé problem [3, 8, 9], which concern thick walled rings. Many papers treat shrink-fit connection as a general problem without specified application [8, 9, 10, 11, 12, 13]. The problems presented in these works differ in the shrink-fit connection loading state. In the paper [10] rotating assembly is analyzed and in [13] the shrink-fit connection

is loaded by the axial force.

In machine design literature, the problem of the thermal field distribution in shrink-fit connections is rarely discussed [4] and in the scientific articles there is lack of thermo-mechanical analysis results concerning shrink-fit connections which can be performed only in the specialized engineering software having advanced contact modelling and multistage analysis facilities. In the literature, the problem of shrinkage mechanism in the shrink-fit connections is also absent.

In this article the experimental data [14], the results from the Finite Element Analysis (FEA), and the results from the theoretical analysis related to the marine crank shaft shrink-fit connection are compared. Assembly of the crank and pin requires introduction of a high thermal load to one of the connected elements, because of the negative geometrical clearance between them. Change in crank hole diameter as a result

* Corresponding author.

E-mail address: r.krol@uthrad.pl (R. Król).

of the thermal load, leads to the positive geometrical clearance between the crank and the pin, which enables joining of the shrink-fit connection without any interference. The connection made this way is inseparable, and any corrections of mistakes occurring during shrinking are impossible after the assembly cools down. For this reason, an important step of the assembly process is the controlled heating of the crank, which makes it possible to obtain a proper temperature. Too low heating up temperature leads to the premature shrinkage, whereas too high heating up temperature causes excessive grain growth and loss of the advantageous mechanical properties of the crank material.

The following types of analysis were performed: (1) shrink-fit connection of the pin and ring (which has regular material distribution around the hole), heated around the hole; (2) shrink-fit connection of the crank and pin with the side or the bottom radiator – crank is heated around the hole; (3) shrink-fit connection without the radiator – crank is heated around the hole; (4) shrink-fit connection without the radiator – crank is heated in furnace.

The main aim of the analyses with the side or the bottom radiator was alignment of the temperature distribution inside the crank hole. For various finite element models (FEM), the maximum torsional moment that the shrink-fit connection can carry was calculated and compared.

2. Experimental set up

The specialized stand was designed for temperature measurement in the shrink-fit connection assembly cycle. Temperature is measured on the surface of the crank at the positions given in Fig. 1a (T1-T8). The assembly cycle includes heating, the placement of the pin in the heated crank hole, and free cooling.

Components of the experimental stand are shown in Figs. 2 and 3. During the measurement process, the crank (2) lies on the supports (8), whose height corresponds to the distance in the scale 1:5 between two cranks of the real shaft. At the bottom side of the crank hole, the gas heating device is mounted (7) supplied from the bottle (1) by the propane-butane gas, whose purpose is to heat the crank up to 350 °C. In the special measurement ring (6) the eight independent temperature sensors (9) are mounted every 45°. The measurement ring is placed on the top surface of the crank. The sensors impose small pressure on the surface of the crank and they are placed around the crank hole. The set of springs guarantees equal alignment of the sensors on the surface of the crank. The electrical isolation between the sensors is made by washers. The steel shields, which are not shown in Figures eliminate measurement errors due to the air flow around the measurement zone. The described stand can measure temperatures with an accuracy of 2%, which was

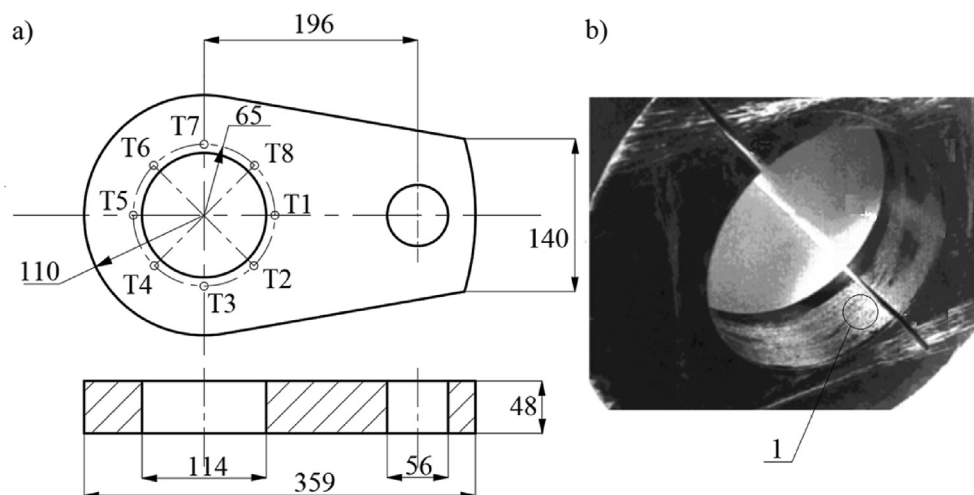


Fig. 1. The dimensions of the crank with the sensors T1-T8 localisation (a) and the dismounted crank with the silver regions (1), which indicate high contact forces in the middle area of the crank hole (b).

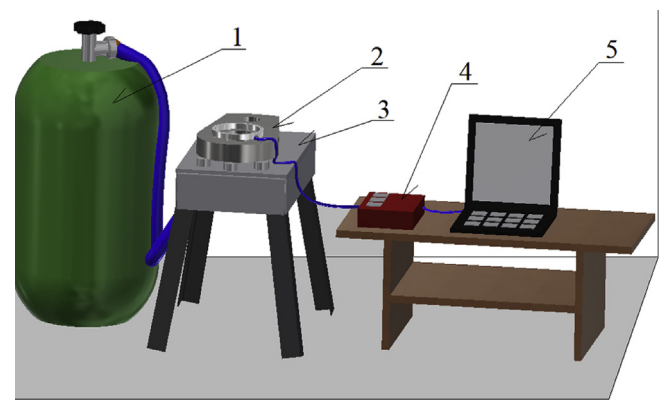


Fig. 2. The measurement stand ready for measurements: gas cylinder (1), crank (2), burner plate with gas burner (3), data acquisition device (4), notebook computer (5).

established on the basis of the comparison of the test measurements.

In Fig. 1b, the dismounted shrink-fit connection is shown. Inside the crank hole silver color (1) designates areas with high contact forces. Experimental stand ready for measurements is shown in Fig. 2. It includes the data acquisition device (4) and the notebook computer (5). The pin (11) shown in Fig. 3 is inserted to the crank (2) when temperature of the point T5 reaches 623 K (350 °C).

3. The finite element analysis

The FEA was performed in the MSC Marc Software. In general, for computations two finite element meshes were prepared – one for the crank and one for the pin. Additional element meshes were prepared for radiators, if one was used in the model. In all of the FEM the geometrical symmetry, and the symmetry of thermal load were used. The mesh of the crank, pin and radiator in the each analysis represents only the half of the geometry of a given object (Fig. 4). Utilisation of the symmetry boundary conditions makes it possible to obtain more accurate analysis because of the higher number of finite elements in the half-model mesh. There are 24300 finite elements in the pin mesh and 13692 finite elements in the crank mesh. In the first stage of analysis (heating up) the pin mesh and the crank mesh overlap. Both the structural and the thermal contact between these meshes at this stage of the analysis are inactive. When the point T5 on the surface of the crank reaches temperature 350 °C, the second stage of analysis begins, and the thermal and structural contact

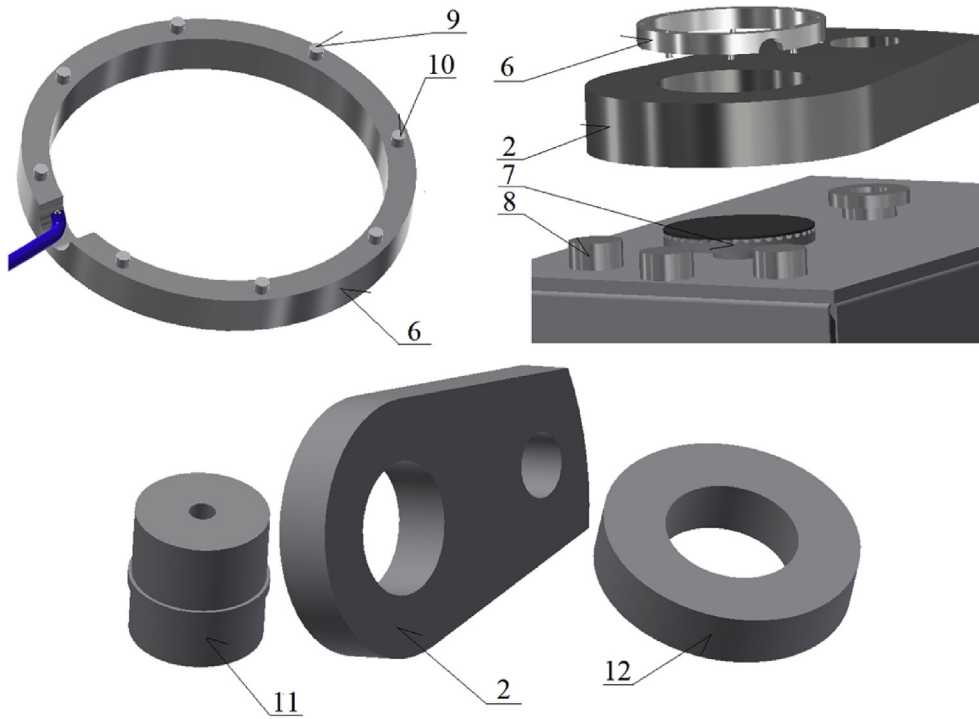


Fig. 3. The measurement stand components: measurement ring (6), gas burner (7), crank supports (8), temperature sensors (9,10) with measurement objects: crank (2), pin (11) and ring (12).

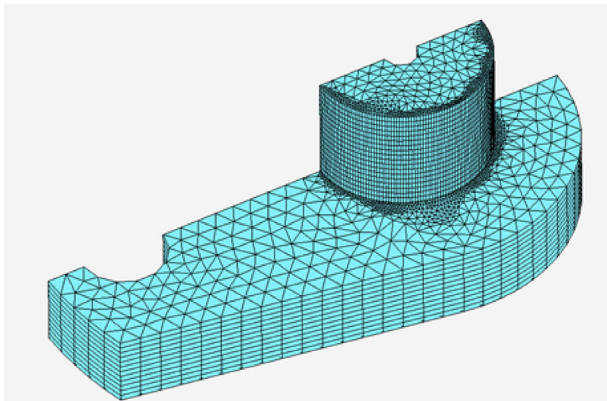


Fig. 4. Finite element mesh of the pin and crank (the half-model with geometric symmetry). Finer mesh can be seen around the shrink-fit connection.

Table 1
Properties of the thermal-structural analysis for the model of the shrink-fit connection without radiators, heated around the crank hole.

Physical entity	Value
Heat transfer coefficient (heating up)	8 W/(m ² ·K)
Heat transfer coefficient (free cooling)	16 W/(m ² ·K)
Temperature at the place of T1 sensor, at the end of heating	563 K (290 °C)
Temperature at the place of T5 sensor, at the end of heating	645 K (372 °C)
Time of the heating up	6000 s (100 min)
Time of the free cooling	24000 s (400 min)

between the pin mesh and the crank mesh is activated. It should be noted, that if the model contains the bottom or the side radiator, the thermal and structural contact between the radiator mesh and the crank mesh is active both in the first and in the second stage of the analysis. At the beginning of the second stage of the analysis there is sufficient geometrical

clearance between the crank and the pin to keep both meshes in separation, without the interference of objects. The properties of the thermal-structural analysis are shown in Tables 1 and 2.

3.1. Boundary conditions

In the FEA, the method of the boundary condition application plays an important role. Improperly applied boundary conditions will influence the stress distribution. Boundary conditions in each stage of the analysis are presented in Figs. 5 and 6. The areas with the thermal face flux boundary conditions are presented in Fig. 5 and marked in yellow. Values of heat flux densities are given in Table 3.

3.2. Thermal analysis

The FEA is a coupled thermal-structural analysis. Alternately with the linear static analysis, the heat transfer analysis is performed according to the governing Eqs. (1), (2), (3), (4), (5), (6), and (7) [15].

$$[B] = \begin{pmatrix} \frac{\partial N_{x_1}}{\partial x_1} & \dots & \frac{\partial N_{x_m}}{\partial x_m} \\ \frac{\partial N_{y_1}}{\partial y_1} & \dots & \frac{\partial N_{y_m}}{\partial y_m} \\ \frac{\partial N_{z_1}}{\partial z_1} & \dots & \frac{\partial N_{z_m}}{\partial z_m} \end{pmatrix}, \tag{1}$$

$$[B]\{T\} = \begin{pmatrix} \frac{\partial N_{x_1}}{\partial x_1} & \dots & \frac{\partial N_{x_m}}{\partial x_m} \\ \frac{\partial N_{y_1}}{\partial y_1} & \dots & \frac{\partial N_{y_m}}{\partial y_m} \\ \frac{\partial N_{z_1}}{\partial z_1} & \dots & \frac{\partial N_{z_m}}{\partial z_m} \end{pmatrix} \cdot \begin{pmatrix} T_1 \\ \dots \\ T_m \end{pmatrix} = \begin{pmatrix} \frac{\partial T}{\partial x} \\ \frac{\partial T}{\partial y} \\ \frac{\partial T}{\partial z} \end{pmatrix}, \tag{2}$$

Table 2
Structural and thermal material parameters used in the analyses as a function of temperature.

Temperature [K] (°C)	Poisson's ratio	Thermal conductivity [W/(m·K)]	Modulus of elasticity [MPa]	Specific heat [J/(kg·K)]	Thermal expansion coefficient [m/(m·K)]
293 (20)	0.3	45.9	212000	461	1.15·10 ⁻⁵
373 (100)	0.3	46.4	207000	496	1.26·10 ⁻⁵
473 (200)	0.3	45.6	199000	533	1.37·10 ⁻⁵
573 (300)	0.3	43.5	192000	568	1.45·10 ⁻⁵
673 (400)	0.3	40.9	184000	611	1.52·10 ⁻⁵

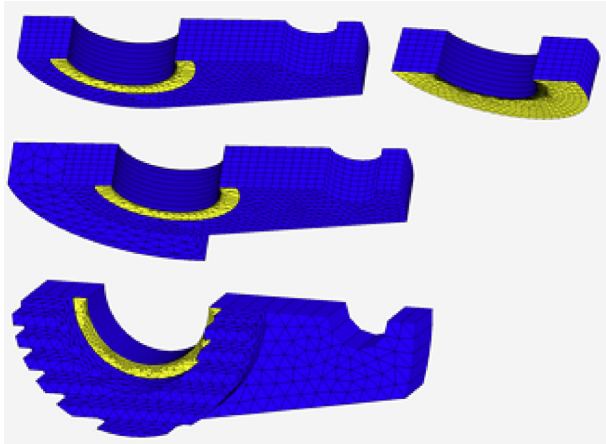


Fig. 5. Faces of the finite elements to which the heat flux load was applied in the various FEM.

$$[C] = \int_V \rho c [N]^T [N] dV, \tag{3}$$

$$[K_c] = \int_V k [B]^T [B] dV, \tag{4}$$

$$\{R_Q\} = \int_V Q [N]^T dV, \tag{5}$$

$$\{R_q\} = \int_S q_s [N]^T dS, \tag{6}$$

$$[C(T)] \cdot \{\dot{T}\} + [K_c(T)] \cdot \{T\} = R_Q(T, t) + R_q(T, t), \tag{7}$$

where: [B] is the temperature-gradient interpolation matrix, $N_{x_i}, N_{y_i}, N_{z_i}$ is the temperature interpolation functions, [T] is the vector of temperature in the nodes (from 1 to m) of the FEM, “m” is the number of nodes in the FEM, [C] is the heat capacity matrix, ρ is density of the FEM bodies, “c” is the heat capacity of the FEM bodies, dV is the volume difference, [K_c] is the thermal-conductivity matrix, “k” is the thermal-conductivity coefficient, [R_Q] and [R_q] is heat flux. \dot{T} is the time derivative of the temperature vector and “t” is time.

The results of the FEM heat transfer analysis for the model of crank and pin without the radiators, heated around the hole and the results of the experimental measurements of the temperatures on the surface of the crank are presented in Figs. 7 and 8.

Table 3
Thermal initial and boundary conditions for analysed FEM.

Physical entity	Value
Initial temperature of the bodies (the crank, the ring, the pin or the radiator)	300 K (27 °C)
Heat flux density in the following models: the crank and the pin without the radiator, the crank with the side radiator and the pin, the crank with the bottom radiator and the pin	150 kW/m ²
Heat flux density in the model of the ring and the pin	21 kW/m ²
Heat flux density in the model of the crank and the pin (the crank heated in a furnace)	6 kW/m ²
The area of FEM faces with applied heat flux in the model of the crank with and without the radiators	0.004184 m ²
The area of FEM faces with applied heat flux in the model with the ring and the pin	0.013875 m ²
The area of FEM faces with applied heat flux in the model of the crank heated in a furnace	0.086801 m ²

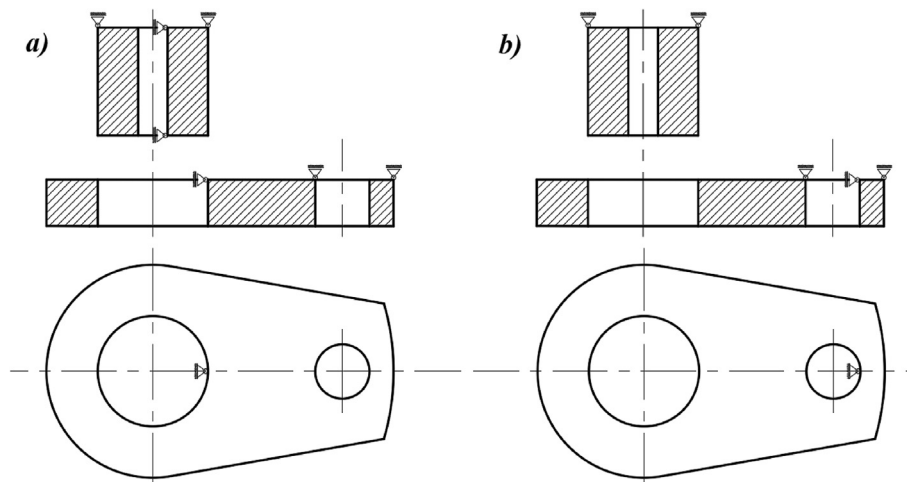


Fig. 6. Boundary conditions in the specified stages of analysis. Supports indicate fixed degrees of freedom. Marked areas indicate places of the application of symmetry boundary conditions. The heating up: figure a), the free cooling: figure b).

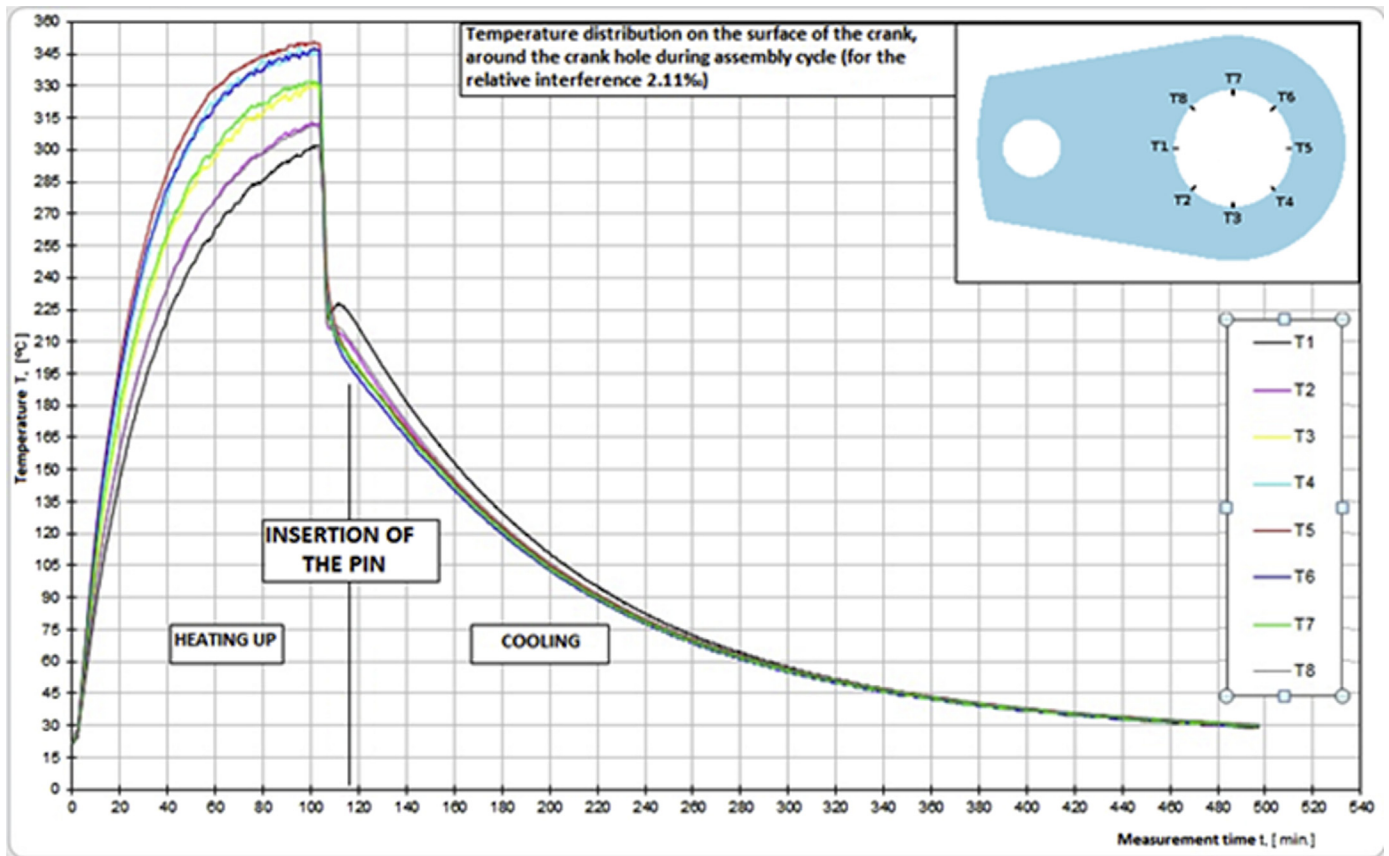


Fig. 7. The temperature measurement data from the experiment for eight sensors (T1-T8).

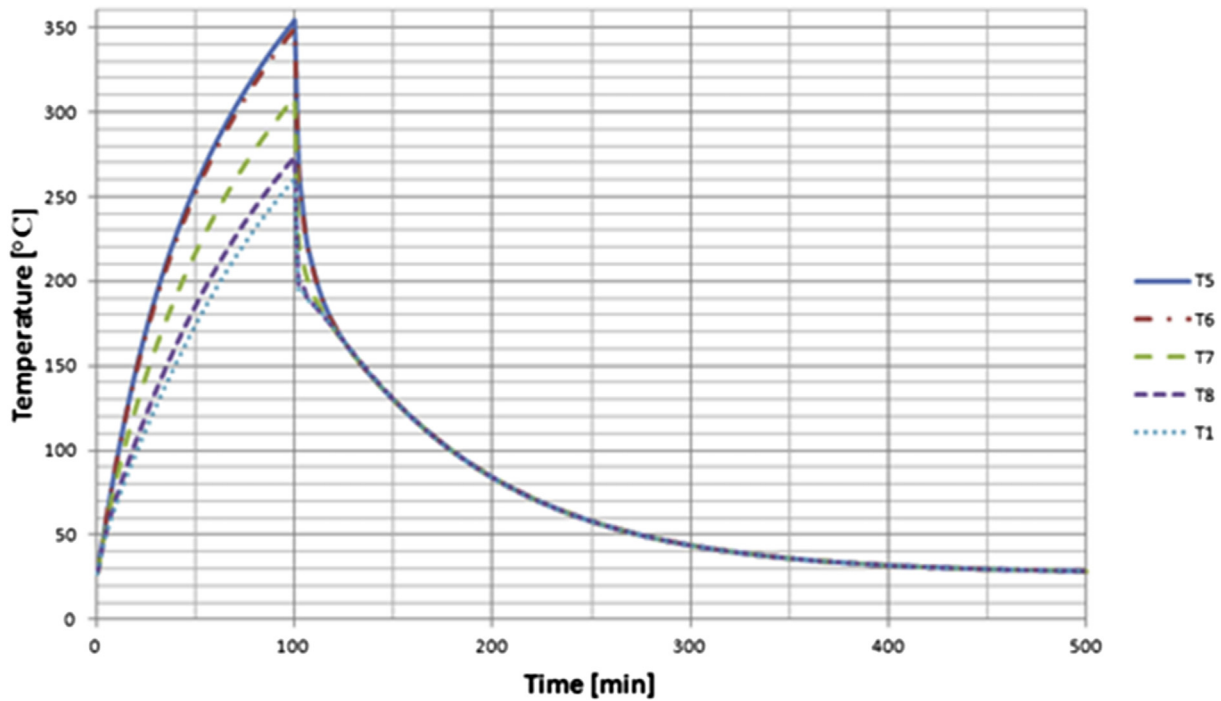


Fig. 8. The results of the FEA. Temperatures at the place of T1, T5, T6, T7 and T8 temperature sensors.

3.3. Structural analysis

In Figs. 9 and 10 radial and circumferential stresses in the crank, measured 5 mm from the shrink-fit connection, is presented. The data

obtained from the FEA was compared with the data from the ultrasonic measurement. Measured stresses are averaged over the thickness of the crank. Fig. 11 presents von Mises stress (calculated on the basis of the radial and circumferential stresses), and Fig. 12 presents contact normal

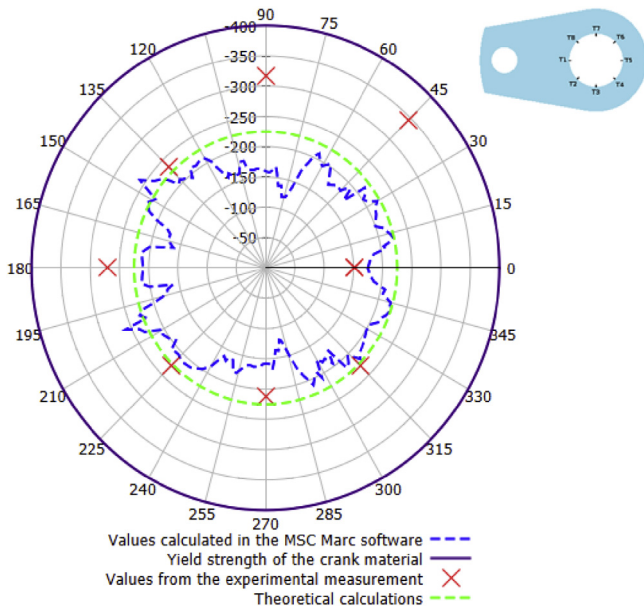


Fig. 9. Radial stresses in the crank.

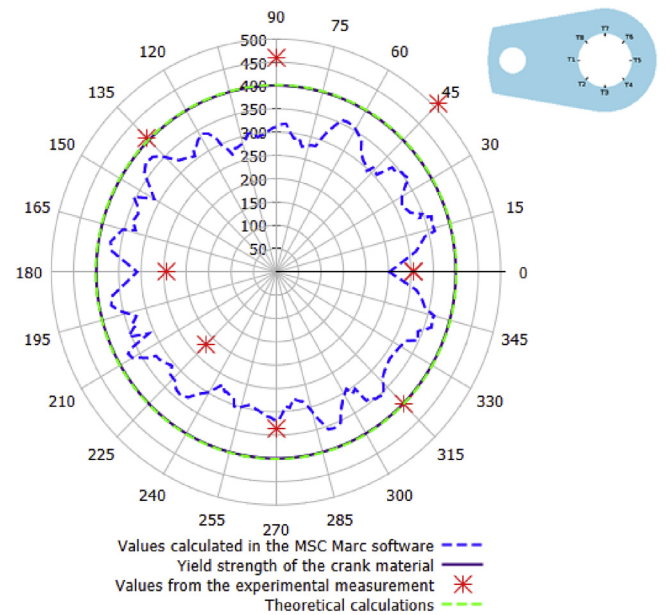


Fig. 11. Von Mises stress in the crank.

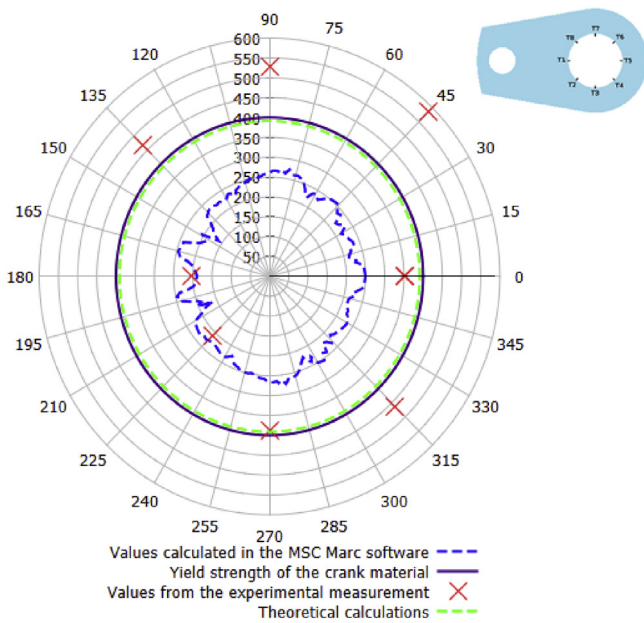


Fig. 10. Circumferential stresses in the crank.

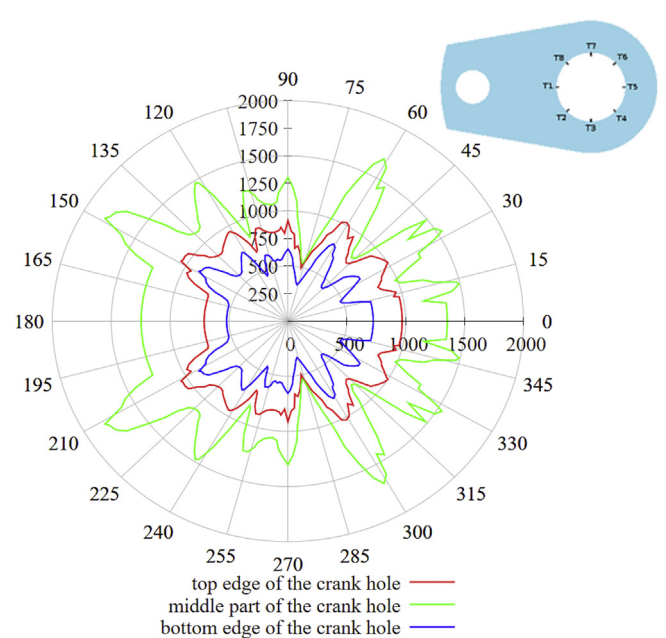


Fig. 12. Contact normal forces on the surface of the crank hole (bottom, middle and top part of the hole).

force in the nodes of the FEM model on the bottom, middle and top part of the crank hole.

4. The theoretical analysis

The main objective of the theoretical analysis is to determine the maximum torsional moment that the shrink-fit connection of the pin and crank can carry, and the radial, circumferential and von Mises stresses on the surface of the crank hole. Calculations were performed on the basis of the Eqs. (8), (9), (10), (11), (12), and (13) [16] with parameter values presented in Table 4. Tables 5 and 6 contain comparison of the theoretical, experimental and FEM calculations.

$$M_{max} = \frac{1}{2} \cdot p_k \cdot \mu \cdot \pi \cdot d^2 \cdot l \tag{8}$$

Table 4
 Parameters for the theoretical calculations.

Parameter	Value
d ₁	23 mm
d ₂	220 mm
d	114 mm
ν ₁	0.3
E ₁	212000 MPa
ν ₂	0.3
E ₂	212000 MPa
μ	0.15
δ	0.00236
l	48 mm
σ _{yield}	400 MPa
E _{pL}	2000 MPa

Table 5

The results of the analyses and experimental measurements for the crank model without the radiator.

	Theoretical calculations	FEM analysis results	Experimental measurements
The maximum torsional moment that connection can be loaded by [Nm]	33140	25443	29900

Table 6

The results of the analyses and experimental measurements (stresses) for the crank model without the radiator.

	Theoretical calculations	FEM analysis results (stresses on the surface of the crank hole)	Experimental measurements (stresses 5 mm from the shrink-fit connection)
Radial stresses [MPa]	-225	- 275 ÷ - 75	- 346 ÷ - 152
Circumferential stresses [MPa]	391	130 ÷ 350	205 ÷ 586
Von Mises stress [MPa]	401	320 ÷ 380	220 ÷ 510

$$p_k = \frac{\delta}{\frac{1}{E_1} \cdot \left(\frac{1+k_1^2}{1-k_1^2} - \nu_1 \right) + \frac{1}{E_2} \cdot \left(\frac{1+k_2^2}{1-k_2^2} - \nu_2 \right)} \quad (9)$$

$$\sigma_{VM} = p_k \cdot \frac{\sqrt{3}}{1 - k_2^2} \quad (10)$$

$$\sigma_{CIR} = p_k \cdot \frac{1 + k_2^2}{1 - k_2^2} \quad (11)$$

$$\sigma_R = p_k \quad (12)$$

$$\sigma_{VM} = \sigma_{yield} + E_{PL} \cdot \epsilon_{PL} \quad (13)$$

where: M_{max} – the maximum torsional moment, the shrink-fit connection can carry, p_k – the pressure on the surface of the crank hole, δ – geometrical interference, d – the diameter of the crank hole, μ – the kinematic friction coefficient, l – length of the shrink-fit connection, E_1, E_2 – Young modulus for the pin and crank material, ν_1, ν_2 – the Poisson number for the pin and crank material, $k_1 = \frac{d_1}{d}$ – the relation of the in-

Table 7

The maximum torsional moment for various methods of heating and various models.

Model type	With side radiator	Heating in furnace	Without the radiators	Ring with coarse mesh	Ring with fine mesh
The maximum torsional moment [Nm]	26 201	25 439	25 443	23 164	23 029

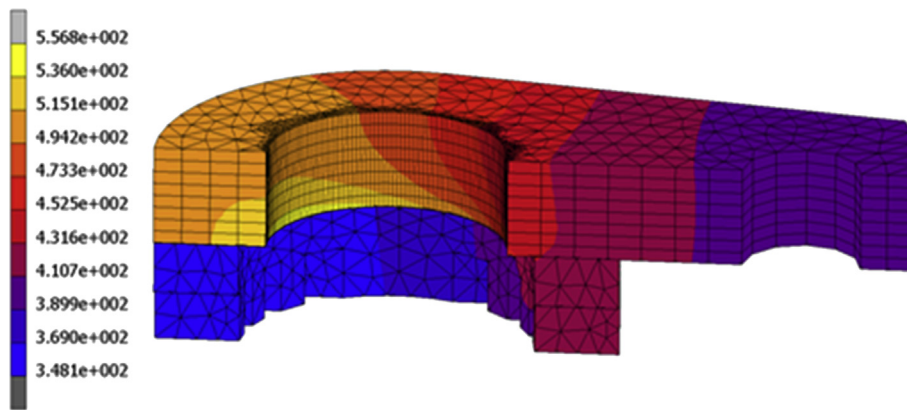


Fig. 13. Irregular temperature distribution [K] in the model with the bottom radiator.

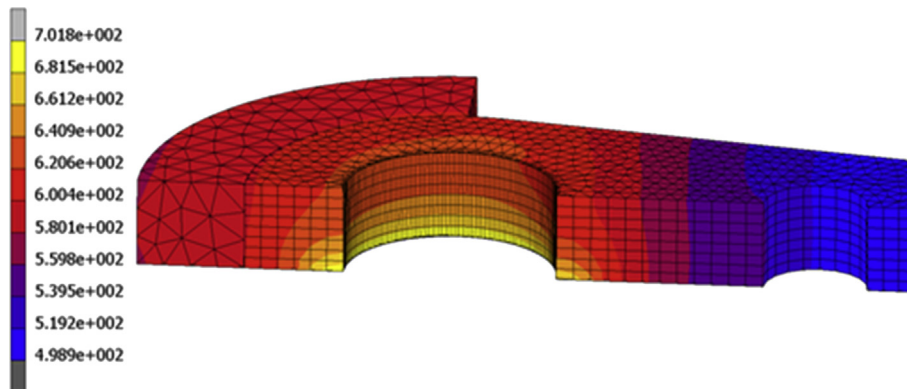


Fig. 14. Regular temperature distribution [K] in the model with the side radiator.

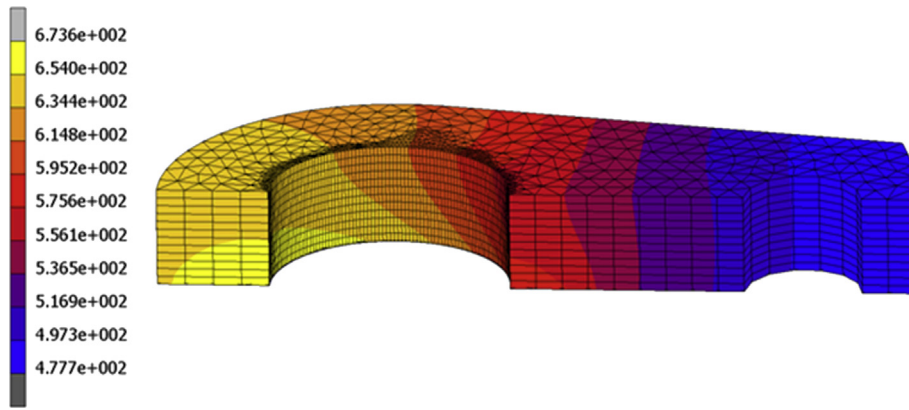


Fig. 15. Irregular temperature distribution [K] in the model without the radiator.

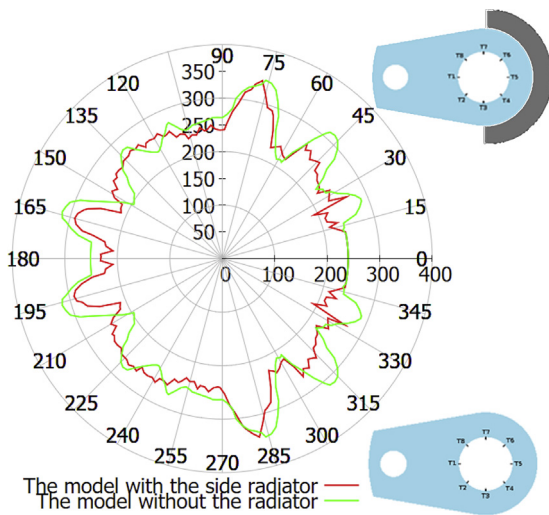


Fig. 16. Circumferential stress in the middle of the crank hole in two FEM.

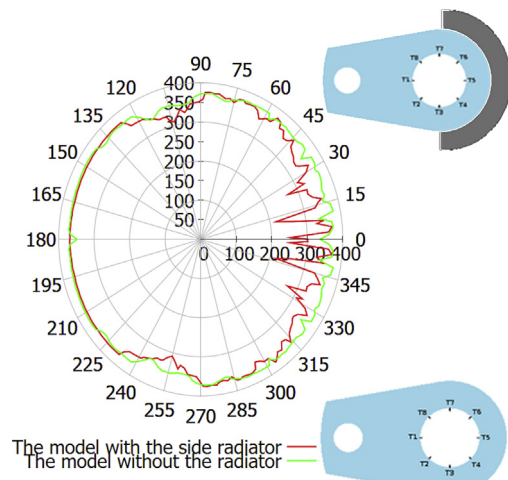


Fig. 18. Von Mises stress in the middle of the crank hole in two FEM.

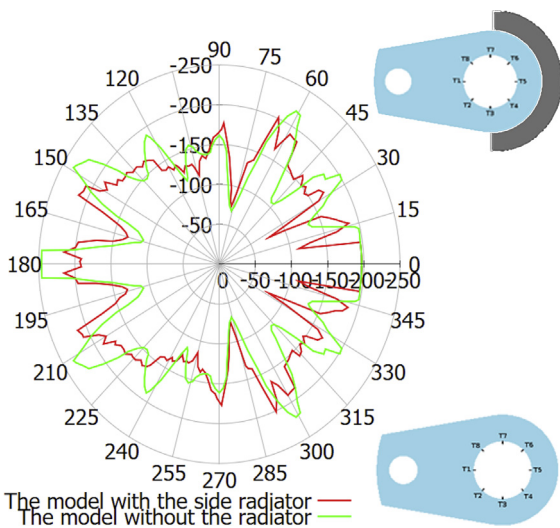


Fig. 17. Radial stress in the middle of the crank hole in two FEM.

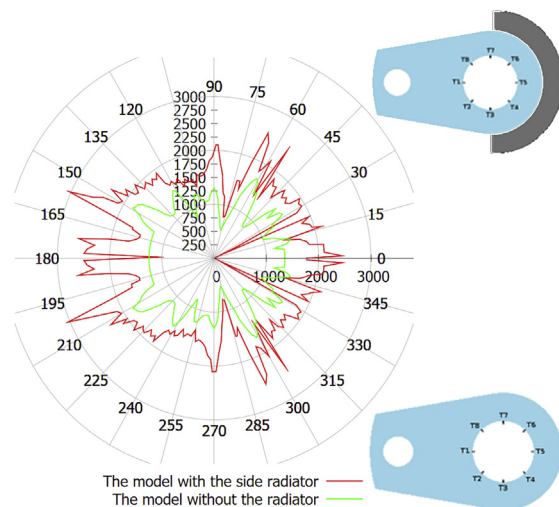


Fig. 19. Contact normal forces in the middle part of the crank hole.

ternal diameter of the pin to the diameter of the crank hole, $k_2 = \frac{d}{d_2}$ – the relation of the diameter of the crank hole to the external diameter of the

stress, σ_{yield} – the yield stress, ϵ_{PL} – plastic strain, E_{PL} – the hardening modulus.

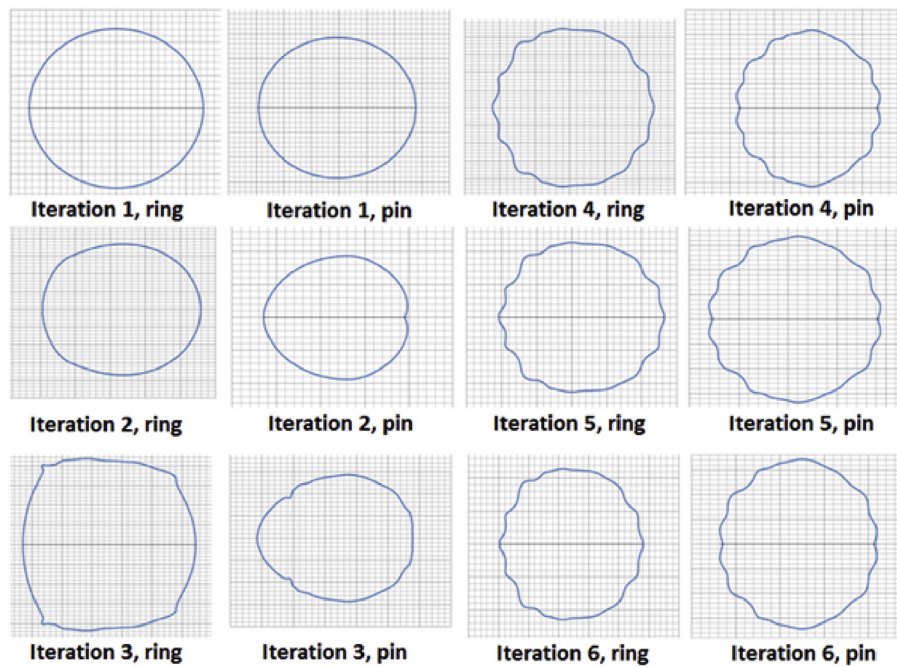


Fig. 20. Shrinkage mechanism for the ring and pin.

5. Influence of the various heating methods on the maximum torsional moment which the shrink-fit connection can be loaded by

The results presented in the previous sections were calculated and measured for the shrink-fit connection without radiators, which was heated around the crank hole only. The aim of the analysis with the radiator was the alignment of the temperature field on the surface of the crank hole. The aligned temperatures should influence the shape of the crank hole during the shrinking process.

Two analyses, for two different heat transfer coefficients were performed with the round radiator attached at the bottom of the crank. There was certain amount of free space near the crank hole to apply the heat flux load. The bottom radiator did not align the temperatures on the surface of the crank hole (Fig. 13). The analysis with the bottom radiator shows that temperatures in the crank, near the hole, are reduced, but the temperature distribution is irregular.

The application of the side radiator made temperature distribution inside the crank hole regular in the circumferential direction, but it changed from the top to the bottom part of the crank hole (Fig. 14). This kind of temperature distribution can guarantee equal shrinking if the pin is placed in the center of the hole, which is difficult to obtain.

The analysis of heating the crank in the furnace was also performed. The heat flux was introduced to each surface of the crank, with the exception of the surfaces to which the symmetry boundary conditions were applied. The results of the performed analyses show that the maximum torsional moment, which the shrink-fit connection can carry, is not dependent on the heating method. The results are presented in Table 7.

In all of the models presented in Table 7, the crank and the ring are heated around the hole, as it was shown in the description to Figs. 2 and 3. The exception is the model heated in the furnace, in which heat flux boundary condition is prescribed to each surface, without the symmetry surfaces. In Table 7, there are two models, which consist of a ring and pin. The model with coarse mesh contains 12028 finite elements (both ring and pin), and the model with the fine mesh contains 20084 finite elements (both ring and pin).

Various temperature distributions at the end of the heating (first stage of the analysis) are presented in Figs. 13, 14 and 15.

6. Stress state on the surface of the crank hole for various models

The authors compared the stress state on the surface of the crank hole in the model of the crank heated in furnace and in the model of the crank heated around the hole, without the radiator. These distributions were nearly the same. The model without the radiator (heated around the hole) was compared also with the model that contain the side radiator. Small differences in the stress distribution were observed in these models. Comparison of the radial, circumferential and von Mises stress distribution in the middle part of the hole for these two models (heated around the crank hole) are shown in Figs. 16, 17 and 18.

The difference between the presented models are the contact normal forces in the middle of the crank hole. Two distributions of the nodal forces are presented in Fig. 19.

7. The shrinkage mechanism

The stress distribution on the surface of the crank or ring hole is created. This state of stress is characteristic for shrink-fit connections. The circumferential stresses in the crank or ring have a positive sign (tension) and the radial stresses have a negative sign (compression) while in the pin, both circumferential and radial stresses have a negative sign. The pin is under compression, and the surface of the pin is going to be created. Shrinkage mechanism of the ring and pin shown in Fig. 20 (inner edge of the ring hole and the outer edge of the pin) indicates that this process is very irregular. The initial position of the pin at the start of shrinking has an influence on the distribution of the stresses and contact normal forces. It should be noted that various methods of heating result in nearly the same values of the maximum torsional moment the connection can carry.

8. Conclusions

Summing up the results, the load capacity of the shrink-fit connection is not dependent on any of the presented heating methods. The differences between the analysed models are up to 2.9% of the obtained solution.

The maximum torsional moment the connection can carry is by 10% higher in the models containing the crank and pin, rather than in models

containing the ring and pin for the same value of the relative interference (2.36 ‰). The value of the maximum torsional moment, that the shrink-fit connection can carry, obtained from the theoretical calculations for the model without the radiators is by 9.8% higher than experimental measurement values. The difference in results can be influenced by the different value of the static friction coefficient in the real model. The 9.8% difference between the theoretical and experimental results proves, that the theoretical equations for the pipe based on the axisymmetric Lamé problem can be used for solving the load capacity and the stress state in the engineering purposes.

In FEA, the maximum value of torsional moment has been obtained for the model with side radiator. Application of the side radiator increases contact forces in the middle of the crank hole (Fig. 19), which makes this solution more beneficial than application of the bottom radiator. FEA analysis also showed that application of side radiator aligns temperature distribution in crank, while the application of bottom radiator causes high circumferential variation of temperature field.

Fig. 12 shows that the highest contact normal forces arise in the middle part of the crank hole. Once the crank was sawed, as it is shown in Fig. 1b, the bright areas indicate the highest values of the contact forces. It is confirmed by the Fig. 1b, that highest contact normal forces occur in the middle of the crank hole, and the distribution of these forces is creased.

The stresses measured at the distance of 5 mm from the shrink-fit connection have more regular distribution than stresses on the surface of the hole. The difference between these values measured with the ultrasonic method, the theoretical and the FEA results are up to 20% of the measured value. Some of the measurement points show high differences in comparison with FEA. The measurement uncertainties could be influenced by the edge effects of ultrasonic measurements or the irregular shape of the crank hole, which could lead to the different interference values.

Declarations

Author contribution statement

Roman Król - Analyzed and interpreted the data; Wrote the paper.

Zbigniew Siemiątkowski - Conceived and designed the experiments; Performed the experiments.

Funding statement

This research utilised the MSC Software National Scientific Software License, operated by the TASK Computer Centre in Gdańsk (Poland). This

license was funded by a computational grant obtained by Kazimierz Pulaski University of Technology and Humanities in Radom, Poland.

Competing interest statement

The authors declare no conflict of interest.

Additional information

Data associated with this study has been deposited at Zenodo under the accession number <https://doi.org/10.5281/zenodo.2577917>.

References

- [1] J. Mydlarz, Undervalued shrink-fit connection, *Proj. i Konstr. inżynierskie* 9 (24) (2009).
- [2] J. Lee, J. Park, Y. Cho, A novel ultrasonic NDE for shrink fit welded structures using interface waves, *Ultrasonics* 68 (May 2016) 1–7.
- [3] O. Eyercioglu, M.A. Kutuk, N.F. Yilmaz, Shrink fit design for precision gear forging dies, *J. Mater. Process. Technol.* 209 (4) (Feb. 2009) 2186–2194.
- [4] C.E. Truman, J.D. Booker, Analysis of a shrink-fit failure on a gear hub/shaft assembly, *Eng. Fail. Anal.* 14 (4) (Jun. 2007) 557–572.
- [5] Z. Siemiątkowski, M. Rucki, S. Lavrynenko, Investigations of the shrink-fitted joints in assembled crankshafts, in: *Proceedings of the 7th International Conference on Mechanics and Materials in Design*, 2017, pp. 1155–1158.
- [6] Z. Siemiątkowski, M. Rucki, S. Lavrynenko, Investigations on the modeled shrink-fitted joints of assembled crankshafts, *J. Mach. Constr. Maint.* 1 (108) (2018) 33–44.
- [7] Z. Siemiątkowski, M. Rucki, J. Kudlacek, Internal stresses analysis in the shrink-fitted joints of the assembled crankshafts, in: *Lecture Notes in Mechanical Engineering*, 2018, pp. 633–640.
- [8] R. Buczkowski, M. Kleiber, A study of the surface roughness in elasto-plastic shrink fitted joint, *Tribol. Int.* 98 (Jun. 2016) 125–132.
- [9] A. Özel, Ş. Temiz, M.D. Aydin, S. Şen, Stress analysis of shrink-fitted joints for various fit forms via finite element method, *Mater. Des.* 26 (4) (Jun. 2005) 281–289.
- [10] N. Antoni, Contact separation and failure analysis of a rotating thermo-elastoplastic shrink-fit assembly, *Appl. Math. Model.* 37 (4) (Feb. 2013) 2352–2363.
- [11] E. Arslan, W. Mack, Shrink fit with solid inclusion and functionally graded hub, *Compos. Struct.* 121 (Mar. 2015) 217–224.
- [12] A. Sackfield, J. Barber, D. Hills, C. Truman, A shrink-fit shaft subject to torsion, *Eur. J. Mech. A Solid.* 21 (1) (Jan. 2002) 73–84.
- [13] J.P. Lopes, D.A. Hills, R.J.H. Paynter, The axisymmetric shrink fit problem subjected to axial force, *Eur. J. Mech. A Solid.* 70 (Jul. 2018) 172–180.
- [14] R. Król and Z. Siemiątkowski, Analysis Files for MSC Marc Finite Element Software, Article: the Analysis of Shrink-Fit Connection – the Methods of Heating and the Factors Influencing the Distribution of Residual Stresses.
- [15] M.S.C. Software, Volume A: theory and user information, in: *MSC Marc User Documentation*, 2012.
- [16] K.F. Aleksandrov, A. Ja, S.A. Ambarcumjan, V.L. Biderman, I.A. Birger, A.S. Volmir, V.M. Darevskij, I.V. Demjanushko, I.G. Kildibekov, L.M. Kurshin, V.M. Makushin, V.I. Rosenbljum, N.G. Savieliev, N.G. Savin, Chernykh, Strength, Stability and Vibration. Handbook in Three Volumes, Mashinostroeniye, Moscow, 1968.